*Journal of Zhejiang University-SCIENCE A (Applied Physics & Engineering)* 2022 23(6):443-457
www.jzus.zju.edu.cn; www.springer.com/journal/11582
E-mail: jzus_a@zju.edu.cn

**Research Article**

https://doi.org/10.1631/jzus.A2100305



# Analysis of dynamic stresses in ballasted railway track due to train passages at high speeds

Jing HU[1]✉, Xue-cheng BIAN[2,3]

[1]*Department of Civil Engineering, Fuzhou University, Fuzhou 350108, China*
[2]*Department of Civil Engineering, Zhejiang University, Hangzhou 310058, China*
[3]*MOE Key Laboratory of Soft Soils and Geoenvironmental Engineering, Zhejiang University, Hangzhou 310058, China*

**Abstract:** Repeated train passages bring detrimental effects on train operations, especially at high speeds. In this study, a computational model consisting of moving train vehicles, track structure, and track foundation is used to investigate the stress distribution in the track substructure and underlying soil, particularly when the train speed approaches the critical speed via 2.5D finite element method. The numerical model has been validated by in-situ test results from a ballasted high-speed railway. The computational results reveal that the substructure is shown to be effective in reducing the stresses transmitted to the ground; however, a simple Boussinesq approximation is proved to be inaccurate because it cannot properly take account of the effect of multi-layered substructures and train speeds. It is acceptable to assume a simplified smooth track in the analysis model for determining the maximum stresses and displacements for a low-speed railway (≤100 km/h) but, for a high-speed one, the dynamic amplification effect of track irregularities must also be considered in subgrade design. Analysis of the stress paths revealed that the load speed and track irregularity increase the likelihood of failure for the subgrade; track irregularity can induce many times of principal stress rotations even under a simple single moving load.

**Key words:** Ballasted railway; Stress analysis; Track irregularity; Stress path; High speed

## 1 Introduction

Ballasted railway track typically consists of the superstructure (e.g., rails, fasteners, and sleepers) and substructure (e.g., ballast and subgrade). Train loads are transmitted through the superstructure and distributed by the substructure into the natural ground below. Of these components, the function of the substructure is to provide support to the track and to reduce the stresses transmitted to the ground in order to avoid excessive settlement.

Historically, the substructure was constructed based on the bearing capacity of different geological conditions. For example, the American Railway Engineering Association (AREA, 1996) assumed an allowable subgrade bearing pressure of 138 kPa for all sub-soil conditions. Some railways were designed using more analytical methods (Raymond, 1978), in which the stresses at the top of the subgrade were often calculated by empirical equations or based on Boussinesq solutions (Selig and Waters, 1994). To control long-term track settlement, more specific and accurate stress conditions are required. British Rail (Heath et al., 1972; Powrie et al., 2007) proposed an approach based on setting a 'threshold stress', determined from cyclic triaxial tests, to avoid excessive plastic deformation during long-term operation. Li and Selig (1998a, 1998b) modified the threshold stress method by taking the track superstructure into account when they calculated the stresses at the top of the subgrade.

Nowadays, the train speed of Japanese Shinkansen is 240–340 km/h and its maximum speed can reach 434 km/h. With the substantial increase in train speeds and axle loads in ballasted railways, the substructure is often confronted with settlement problems because of the increasing superimposed stress transferred into the subgrade (Li et al., 2018). Dynamic finite element (FE) analyses have shown that a static analysis is not

✉ Jing HU, jingh@fzu.edu.cn
Xue-cheng BIAN, https://orcid.org/0000-0003-2143-0512

Received July 2, 2021; Revision accepted Jan. 11, 2022;
Crosschecked Apr. 23, 2022

sufficiently accurate for high-speed train loading (Heath et al., 1972; Powrie et al., 2008; Yang et al., 2009; Hu et al., 2016; Varandas et al., 2016; Ngo et al., 2017). Of particular concern is the significant vibration amplification that occurs when the train speed approaches the critical speed related to the wave speed in the ground (Takemiya, 2003; Auersch, 2008; Yang et al., 2009; Bian et al., 2016; Hu et al., 2016; Sayeed and Shahin, 2016). However, analysis of the stresses in the subgrade with particular reference to the critical speed is rare. To the authors' knowledge, only Yang et al. (2009) carried out a study into the effect of train speed on the stress by means of a 2D dynamic FE analysis. Their study revealed the dramatic amplification effect on stresses when the train exceeded the critical speed.

Soil subjected to traffic loads usually undergoes cyclic principal stress rotation. The rotation of the principal stress axes has a considerable effect on the deformation behavior of soil (Ishihara and Towhata, 1983; Cai Y et al., 2013; Xiao et al., 2014; Cai YQ et al., 2017). Track irregularity will also cause stress changes in the subgrade and ground (Yang et al., 2009). However, the principal stress rotation under loading at critical speeds has rarely been discussed; the effect of track irregularity on principal stress rotation also has not been investigated.

It is therefore of the utmost importance to gain a better understanding of the dynamic stress responses and principal stress rotation behavior of track substructures under train traffic loads at high speeds taking into account track irregularity. In this paper, a numerical model is proposed, based on the 2.5D FE method. This incorporates a ballasted railway track, substructure, and natural ground, and allows the dynamic stress response of a high-speed ballasted railway track to be determined. Field measurements on a ballasted high-speed railway (HSR) in the northern part of China (Qin-Shen HSR) are used to validate the proposed analysis model. After the validation with field measurements, the model is used to explore the dynamic stress response with special reference to the critical speed. To gain further insights into the dynamic stress transmission within the subgrade and sub-soil, the dynamic stress distribution and its development with increasing train speed are discussed. The management standard used by the Japanese Shinkansen for longitudinal track irregularity is used in the model to investigate the long-term dynamic response characteristics of ballasted track and the influence of track irregularity on the principal stress rotation.

## 2 Modelling of track-substructure-ground system for ballasted track under train moving loads

### 2.1 Modelling of track-substructure system

An illustrative diagram of the track-substructure-ground analysis model is presented in Fig. 1a. The track superstructure, together with underlying substructure and ground, is aligned in the $x$-direction, and they are assumed to be infinite and invariant in this direction. A more detailed model of the track is given in Fig. 1b. As only symmetric vertical loading is considered, the two rails are modeled as a single Euler beam with mass per unit length $m_r$ and bending stiffness $EI_r$ (MN·m$^2$). The sleepers are modeled as a distributed mass $m_s$ per unit length of track. The rails and sleepers are connected by rail pads, which are modeled as vertical spring stiffness $k_p$ (MN/m$^2$) and dashpots $c_p$ (MN·s/m$^2$). In the practice, the ballast layer has a

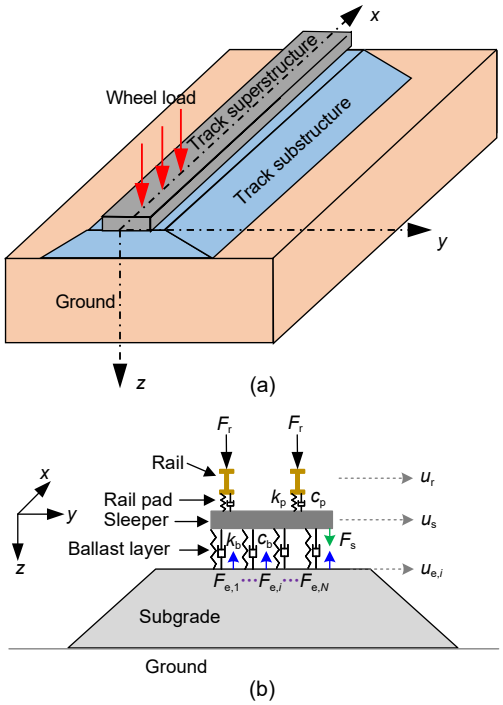


**Fig. 1 Schematic view of track-substructure-ground model: (a) track-substructure-ground system; (b) track details. The parameters are explained in the text**

certain elasticity which makes the train-induced discrete load that is transferred from the sleepers more uniform at the subgrade. According to Sheng et al. (1999), the load distribution at the subgrade surface can be treated as uniform along the *x*-direction by simplifying the ballasted layer as a viscoelastic layer with a width $d$ and a mass per unit length of track $m_b$; only the vertical spring stiffness $k_b$ (MN/m$^2$) and damping $c_b$ (MN·s/m$^2$) of the ballasted layer are taken into account.

The governing equation of the rail beam in vertical motion is given as follows:

$$EI_r\frac{\partial^4 u_r}{\partial x^4}+m_r\frac{\partial^2 u_r}{\partial t^2}+\left(k_p+c_p\frac{\partial}{\partial t}\right)\left(u_r-u_s\right)=F_r(t)\delta(x-ct), \tag{1}$$

where $u_r$ is the rail displacement, $t$ is the time, $F_r$ is the interaction force at the rail surface which is moving with a speed $c$, $u_s$ is the displacement of the sleeper, and $\delta$ is the Dirac-delta function.

For the sleeper mass,

$$m_s\frac{\partial^2 u_s}{\partial t^2}+\left(k_p+c_p\frac{\partial}{\partial t}\right)\left(u_s-u_r\right)=-F_s, \tag{2}$$

where $F_s$ is the interaction force (per unit length) between the ballast and the sleeper.

The ballast layer is divided into $N$ slices in the transverse direction. A linear spring stiffness with a consistent mass distribution is used to approximate the behavior of the ballast layer:

$$\sum_{i=1}^{N}\frac{m_b}{6N}\left(2\frac{\partial^2 u_s}{\partial t^2}+\frac{\partial^2 u_{e,i}}{\partial t^2}\right)+\sum_{i=1}^{N}\frac{1}{N}\left(k_b+c_b\frac{\partial}{\partial t}\right)\left(u_s-u_{e,i}\right)=F_s, \tag{3}$$

$$\frac{m_b}{6N}\left(\frac{\partial^2 u_s}{\partial t^2}+2\frac{\partial^2 u_{e,i}}{\partial t^2}\right)+\frac{1}{N}\left(k_b+c_b\frac{\partial}{\partial t}\right)\left(u_{e,i}-u_s\right)=-F_{e,i},\quad i=1,\ 2,\ \cdots,\ N, \tag{4}$$

where $N$ is the number of slices in the track's transverse direction at the surface of the subgrade; $F_{e,i}$ and $u_{e,i}$ are the interaction force and displacement at the $i$th interface node of the ballasted layer and subgrade surface, respectively.

As the geometry and material properties are assumed not to vary in the *x*-direction, i.e. along the axis of the track, Eqs. (1)–(4) are solved using the Fourier transform method. The Fourier transform of displacement $u(x, y, z, t)$ and its inverse transform are defined by:

$$\tilde{\tilde{u}}\left(\xi_x,\ y,\ z,\ \omega\right)=\int_{-\infty}^{+\infty}\int_{-\infty}^{+\infty}u(x,\ y,\ z,\ t)\mathrm{e}^{\mathrm{i}\xi_x x}\mathrm{e}^{-\mathrm{i}\omega t}\mathrm{d}x\mathrm{d}t, \tag{5}$$

$$u(x,\ y,\ z,\ t)=\frac{1}{4\pi^2}\int_{-\infty}^{+\infty}\int_{-\infty}^{+\infty}\tilde{\tilde{u}}\left(\xi_x,\ y,\ z,\ \omega\right)\mathrm{e}^{-\mathrm{i}\xi_x x}\mathrm{e}^{\mathrm{i}\omega t}\mathrm{d}\xi_x\mathrm{d}\omega, \tag{6}$$

where $(y, z)$ denote the transverse and vertical coordinates normal to the *x*-direction, $\omega$ is the circular frequency, and $\xi_x$ is the horizontal wavenumber relevant to the *x*-direction. '–' and '~' above a variable indicate components in the wavenumber and frequency domains, respectively (Bian et al., 2019).

Applying the Fourier transform to Eqs. (1)–(4) yields the following (Nussbaumer, 1981):

$$\left(EI_r\xi_x^4-m_r\omega^2+k_p+\mathrm{i}\omega c_p\right)\tilde{\tilde{u}}_r-\left(k_p+\mathrm{i}\omega c_p\right)\tilde{\tilde{u}}_s=\tilde{\tilde{F}}_r\left(\xi_x,\ \omega\right), \tag{7}$$

$$\left(k_p+\mathrm{i}\omega c_p-m_s\omega^2\right)\tilde{\tilde{u}}_s-\left(k_p+\mathrm{i}\omega c_p\right)\tilde{\tilde{u}}_r=-\tilde{\tilde{F}}_s\left(\xi_x,\ \omega\right), \tag{8}$$

$$\sum_{i=1}^{N}\left[\left(\frac{k_b+\mathrm{i}\omega c_b}{N}-\frac{m_b\omega^2}{3N}\right)\tilde{\tilde{u}}_s-\left(\frac{m_b\omega^2}{6N}+\frac{k_b+\mathrm{i}\omega c_b}{N}\right)\tilde{\tilde{u}}_{e,i}\right]=\tilde{\tilde{F}}_s\left(\xi_x,\ \omega\right), \tag{9}$$

$$\left(\frac{k_b+\mathrm{i}\omega c_b}{N}-\frac{m_b\omega^2}{3N}\right)\tilde{\tilde{u}}_{e,i}-\left(\frac{m_b\omega^2}{6N}+\frac{k_b+\mathrm{i}\omega c_b}{N}\right)\tilde{\tilde{u}}_s=-\tilde{\tilde{F}}_{e,i}\left(\xi_x,\ \omega\right),\quad i=1,\ 2,\ \cdots,\ N. \tag{10}$$

Writing

$$T_1=EI_r\xi_x^4-m_r\omega^2+k_p+\mathrm{i}\omega c_p,$$

$$T_2=k_p+\mathrm{i}\omega c_p,$$

$$T_3=k_p+\mathrm{i}\omega c_p-m_s\omega^2,$$

$$T_4=\frac{k_b+\mathrm{i}\omega c_b}{N}-\frac{m_b\omega^2}{3N},$$

$$T_5=\frac{m_b\omega^2}{6N}+\frac{k_b+\mathrm{i}\omega c_b}{N},$$

Eqs. (7)–(10) can be reduced to the following form:

$$T_4\tilde{\tilde{u}}_{e,i}+\frac{T_1(T_4^2-T_5^2)}{T_1T_3-T_2^2}\sum_{i=1}^{N}\tilde{\tilde{u}}_{e,i}=-\tilde{\tilde{F}}_{e,i}+\frac{T_2T_5-T_1T_4}{T_1T_3-T_2^2}\tilde{\tilde{F}}_r(\xi_x,\ \omega). \tag{11}$$

Then, writing

$$A=\frac{k_b+\mathrm{i}\omega c_b}{N}-\frac{m_b\omega^2}{3N},$$

$$B=(EI_r\beta^4-m_r\omega^2+k_p+\mathrm{i}\omega c_p)\times\left[\left(\frac{k_b+\mathrm{i}\omega c_b}{N}-\frac{m_b\omega^2}{3N}\right)^2-\left(\frac{m_b\omega^2}{6N}+\frac{k_b+\mathrm{i}\omega c_b}{N}\right)^2\right]\Big/\left[(EI_r\beta^4-m_r\omega^2+k_p+\mathrm{i}\omega c_p)(k_p+\mathrm{i}\omega c_p-m_s\omega^2)-(k_p+\mathrm{i}\omega c_p)^2\right],$$

$$G=(k_p+\mathrm{i}\omega c_p)\left(\frac{m_b\omega^2}{6N}+\frac{k_b+\mathrm{i}\omega c_b}{N}\right)\Big/\left[(EI_r\beta^4-m_r\omega^2+k_p+\mathrm{i}\omega c_p)(k_p+\mathrm{i}\omega c_p-m_s\omega^2)-(k_p+\mathrm{i}\omega c_p)^2\right]-(EI_r\beta^4-m_r\omega^2+k_p+\mathrm{i}\omega c_p)\times\left(\frac{k_b+\mathrm{i}\omega c_b}{N}-\frac{m_b\omega^2}{3N}\right)\Big/\left[(EI_r\beta^4-m_r\omega^2+k_p+\mathrm{i}\omega c_p)\times(k_p+\mathrm{i}\omega c_p-m_s\omega^2)-(k_p+\mathrm{i}\omega c_p)^2\right],$$

Eq. (11) can be rewritten as:

$$A\tilde{\tilde{u}}_{e,i}+B\sum_{i=1}^{N}\tilde{\tilde{u}}_{e,i}=-\tilde{\tilde{F}}_{e,i}+G\tilde{\tilde{F}}_r(\xi_x,\ \omega). \tag{12}$$

Eq. (12) can be written in matrix form as follows:

$$\boldsymbol{D}\tilde{\tilde{\boldsymbol{U}}}_e=-\tilde{\tilde{\boldsymbol{F}}}_E+G\tilde{\tilde{\boldsymbol{F}}}_R, \tag{13}$$

where

$$\tilde{\tilde{\boldsymbol{U}}}_e=\left[\tilde{\tilde{u}}_{e,1},\ \tilde{\tilde{u}}_{e,2},\ \cdots,\ \tilde{\tilde{u}}_{e,N}\right]^{\mathrm{T}},$$

$$\tilde{\tilde{\boldsymbol{F}}}_E=\left[\tilde{\tilde{F}}_{e,1},\ \tilde{\tilde{F}}_{e,2},\ \cdots,\ \tilde{\tilde{F}}_{e,N}\right]^{\mathrm{T}},$$

$$\tilde{\tilde{\boldsymbol{F}}}_R=\left[\tilde{\tilde{F}}_r,\ \tilde{\tilde{F}}_r,\ \cdots,\ \tilde{\tilde{F}}_r\right]_N^{\mathrm{T}},$$

and the elements of $\boldsymbol{D}$ are given by

$$D_{ij}=\begin{cases}A+B, & i=j,\\ B, & i\neq j,\end{cases}$$

$$i=1,\ 2,\ \cdots,\ N,\ j=1,\ 2,\ \cdots,\ N.$$

### 2.2 2.5D finite element modelling of subgrade-ground system

With the introduction of the 2.5D FE model, the cross-section of the subgrade-ground system is meshed by 2D FEs (Yang and Hung, 2001; Bian et al., 2012, 2016; Hu et al., 2019). Using the Fourier transform defined in Eqs. (5) and (6), the third coordinate in the $x$-direction (track direction) is replaced by the wavenumber $\xi_x$. After introducing the element shape functions, the discretized form of the governing equation in the frequency domain can be derived in a similar way to the conventional FE method (Brenner and Scott, 2008):

$$(\boldsymbol{K}-\omega^2\boldsymbol{M})\tilde{\tilde{\boldsymbol{U}}}=\tilde{\tilde{\boldsymbol{F}}}, \tag{14}$$

where $\boldsymbol{M}$ and $\boldsymbol{K}$ are the mass and stiffness matrices of the subgrade-ground system, respectively, and $\boldsymbol{U}$ is the vector of nodal displacements. Detailed expressions for $\boldsymbol{M}$ and $\boldsymbol{K}$ have already been given by Bian et al. (2019). $\boldsymbol{F}$ is the load applied on the subgrade surface, which is equal to $\boldsymbol{F}_E$, i.e.,

$$-\tilde{\tilde{\boldsymbol{F}}}_E=-\tilde{\tilde{\boldsymbol{F}}}. \tag{15}$$

### 2.3 Mathematical description of the forces on the rails

The passage of a train can be simulated by a series of moving axle loads corresponding to the train geometry in Fig. 2.

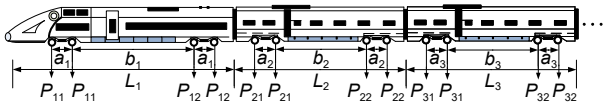


**Fig. 2 Geometric profile of train wheel loads. The parameters are explained in the text**

For a train comprising $M$ vehicles, the successive axle loads moving with a constant velocity $c$ can be represented using the quarter car model proposed by Takemiya and Bian (2005):

$$\tilde{\tilde{F}}_{\mathrm{r}}\left(\xi_x,\,\omega\right)=\sum_{n=1}^{M}\tilde{\tilde{P}}_n\left(\xi_x,\,\omega\right),\tag{16}$$

where $P_n$ represents the wheel loads of the $n$th vehicle, which is given by

$$\tilde{\tilde{P}}_n\left(\xi_x,\,\omega\right)=\sum_{i=1}^{4}\left(\mathrm{e}^{-\mathrm{i}\xi_x x_{ni}}\right)\tilde{\tilde{P}}_{ni}\left(\xi_x,\,\omega\right),\tag{17}$$

in which

$$\begin{aligned}x_{n1}&=\sum_{n=1}^{M}L_n+x_0,\\ x_{n2}&=a_n+\sum_{n=1}^{M}L_n+x_0,\\ x_{n3}&=a_n+b_n+\sum_{n=1}^{M}L_n+x_0,\\ x_{n4}&=2a_n+b_n+\sum_{n=1}^{M}L_n+x_0,\end{aligned}$$

where $P_{n1}$, $P_{n2}$, $P_{n3}$, and $P_{n4}$ are the axle loads for the four wheelsets of the $n$th vehicle, respectively. $x_0$ is the distance to the first axle load position. As indicated in Fig. 2, $L_n$ is the length of the $n$th vehicle, $a_n$ is the length of the bogie wheelbase of the $n$th vehicle, and $b_n$ is the distance from the second axle to the third axle of the $n$th vehicle.

Track irregularities have a direct impact on the interaction forces at the rail surface. For irregularities at the rail surface defined as a single cosine distribution, Bian et al. (2011) derived the mathematical expression for $F_{\mathrm{r}}$ due to a single cosine rail irregularity. If the longitudinal track irregularity is described by a power spectral density (PSD), the trigonometric series method can be used to convert the PSD to a spatial distribution, and obtain the interaction forces at the rail surface during the passage of a train (Bian et al., 2015):

$$\begin{aligned}&\tilde{\tilde{F}}_{\mathrm{r}}\left(\xi_x,\,\omega\right)=\\ &\sum_{n=1}^{M}\tilde{\tilde{P}}_n\left(\xi_x,\,\omega\right)=\delta\left(\xi_x-\frac{\omega}{c}\right)R_1\left(\xi_x\right)+\\ &\sum_{j=1}^{Z}\delta\left(\xi_x-\frac{\omega-\omega_j}{c}\right)R_2\left(\xi_x\right)+\\ &\sum_{j=1}^{Z}\delta\left(\xi_x-\frac{\omega+\omega_j}{c}\right)R_3\left(\xi_x\right),\end{aligned}\tag{18}$$

where $Z$ is the total number of cosine waves included. The detailed expressions for $R_1$, $R_2$, and $R_3$ can be found in reference (Bian et al., 2015).

### 2.4 Coupling of track-substructure-ground motions

Introducing Eqs. (15) and (18) into Eq. (13), then adding Eq. (13) to Eq. (14), by eliminating $\boldsymbol{F}_{\mathrm{E}}$, the governing equation of track-substructure-ground motions can be derived as:

$$\boldsymbol{D}\tilde{\tilde{\boldsymbol{U}}}_{\mathrm{e}}+\left(\boldsymbol{K}-\omega^2\boldsymbol{M}\right)\tilde{\tilde{\boldsymbol{U}}}=G\tilde{\tilde{\boldsymbol{F}}}_{\mathrm{R}}.\tag{19}$$

The displacement $u_{\mathrm{e}}$ of the nodes at the subgrade surface should be consistent with the displacement of the corresponding contact node of the subgrade-ground system. Thus, the dynamic governing equation of ballasted railway track substructure ground system can be written as:

$$\left[\boldsymbol{K}-\omega^2\boldsymbol{M}\quad\boldsymbol{K}-\omega^2\boldsymbol{M}\quad\boldsymbol{K}-\omega^2\boldsymbol{M}+\boldsymbol{D}\right]\begin{bmatrix}\tilde{\tilde{\boldsymbol{U}}}_x\\ \tilde{\tilde{\boldsymbol{U}}}_y\\ \tilde{\tilde{\boldsymbol{U}}}_z\end{bmatrix}=\begin{bmatrix}0\\0\\G\tilde{\tilde{\boldsymbol{F}}}_{\mathrm{R}}\end{bmatrix}.\tag{20}$$

## 3 Verification of the proposed 2.5D finite element model by field measurements

In this section, the dynamic response of the track-substructure-ground system subjected to train traffic loads is investigated using the 2.5D FE numerical model and compared with existing field measurements.

### 3.1 Overview of the field test

In 2003, a field test on a newly-built ballasted high-speed railway, Qin-Shen HSR, was conducted (Nie, 2005; Nie et al., 2005). The total length of this line is 404 km, the design speed was 300 km/h, and the operating speed was around 250 km/h. In the field tests, dynamic soil pressure sensors were buried in the track substructure to record the dynamic stresses transmitted through the superstructure to the substructure during train passages at different train speeds. Three dynamic soil pressure sensors were placed at the top of the sub-ballast layer and three at the top of the subgrade, all beneath the sleepers, as shown in Fig. 3. At each depth, the three sensors were located at the track edge, at the track center, and directly beneath the rail, respectively.

The test train was a “Pioneer” train with six vehicles. It has the same geometry of wheel axle

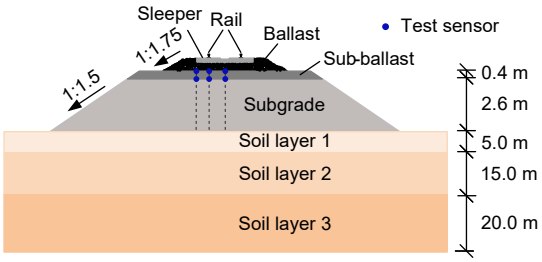


**Fig. 3 Geometry of substructure and underlying soil of Qin-Shen HSR with sensor installation (Nie, 2005)**

distribution as is depicted in Fig. 2. The vehicle length ($l$) is 26 m, the distance between the second and third axles ($b$) is 18 m, and the bogie wheelbase ($a$) is 2.5 m. The parameters used for the multi-body model of each vehicle are shown in Table 1.

**Table 1 Parameters of the "Pioneer" train (Nie, 2005)**

| Parameter | Value |
|---|---|
| Mass of car body (kg) | 40240 |
| Mass of the bogie (kg) | 3000 |
| Mass of the wheelsets (kg) | 1500 |
| Stiffness of the primary suspension (MN/m) | 2.5 |
| Damping of the primary suspension (MN·s/m) | 0.2 |
| Stiffness of the secondary suspension (MN/m) | 1.87 |
| Damping of the secondary suspension (MN·s/m) | 0.42 |

### 3.2 2.5D numerical modelling of Qin-Shen HSR

In the model of the Qin-Shen HSR, the ballast was simplified as a layer of continuous springs supporting the sleepers with specific stiffness and mass per unit length. The sub-ballast layer, subgrade, and underlying soils were modeled by 2.5D FEs. The measured track irregularity PSD of the Qin-Shen HSR (Jin et al., 2008) is represented using 200 cosine functions based on the trigonometric series method (Shinozuka, 2005). Since the model is linearly elastic, the track irregularity PSD can be approximated by the sum of the responses of the 200 cosine functions.

Parameters describing the physical properties of the track superstructure are shown in Table 2, and those for the substructure and underlying ground are shown in Table 3.

**Table 2 Properties of track superstructure in Qin-Shen HSR (for two rails)**

| Parameter | Value |
|---|---|
| Mass of rail beam per unit length of track (kg/m) | 120 |
| Bending stiffness of rail beam (MN·m$^2$) | 13.24 |
| Mass of sleeper per unit length of track (kg/m) (Sheng et al., 1999) | 490 |
| Rail pad stiffness (MN/m$^2$) (Choi, 2014) | 270 |
| Rail pad damping (kN·s/m$^2$) (Choi, 2014) | 83.5 |
| Contact width of railway and foundation (m) | 2.6 |

The cross-section of the track-substructure-ground model is shown schematically in Fig. 4. The substructure and ground are modelled as single-phase elastic solids, with the parameters summarized in Table 3. The depth of this model is 60 m and its width is 100 m. The maximum element size in the central area (40-m width and 30-m depth) of the mesh in Fig. 4 is 0.5 m× 0.5 m. To prevent wave reflection back into the model from the boundaries of the finite domain, the multilayer damping boundary approach developed by Liu and Jerry (2003) is adopted. The total thickness of the damped layers at the edges and bottom of the model is 20 m.

### 3.3 Verification of dynamic stress responses

The time-histories of the dynamic vertical stress responses beneath the rail at the top of the sub-ballast layer under the "Pioneer" train are shown in Fig. 5 for train speeds of 160 km/h and 250 km/h. Both results are in close agreement with the field measurements.

**Table 3 Properties of substructure and underlying soil in Qin-Shen HSR (Nie, 2005)**

| Item | Thickness (m) | Density (kg/m$^3$) | Shear wave velocity, $V_s$ (m/s) | Poisson's ratio | Mass (kg/m) | Stiffness (MN/m$^2$) | Damping |
|---|---|---|---|---|---|---|---|
| Ballast layer (Sheng et al., 1999) | | | | | 1200 | 315 | 0.33 MN·s/m$^2$ |
| Sub-ballast | 0.4 | 2150 | 251 | 0.25 | | | 0.03 |
| Subgrade | 2.6 | 2000 | 190 | 0.30 | | | 0.04 |
| Soil layer 1 | 5.0 | 1900 | 110 | 0.35 | | | 0.05 |
| Soil layer 2 | 15.0 | 1800 | 120 | 0.35 | | | 0.05 |
| Soil layer 3 | 20.0 | 1850 | 128 | 0.35 | | | 0.05 |

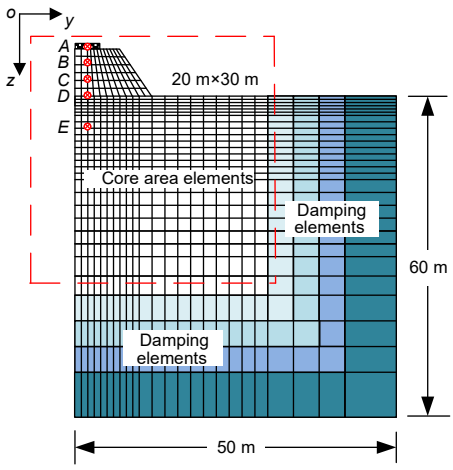


**Fig. 4 Schematic view of half of the FE model of the track-substructure-ground system of Qin-Shen HSR (not to scale)**

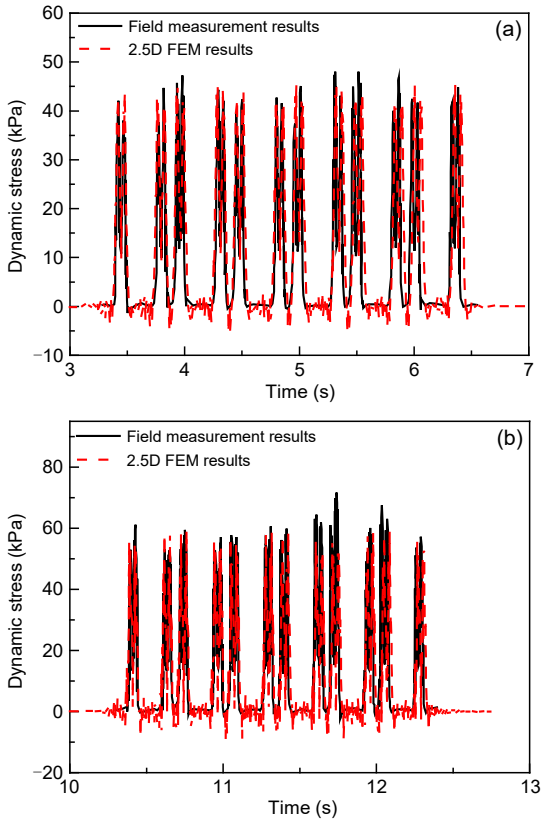


**Fig. 5 Time-histories of dynamic vertical stresses beneath the rail at the top of the sub-ballast layer: (a) $c$=160 km/h; (b) $c$=250 km/h**

## 4 Numerical analysis

To obtain more general conclusions on the dynamic stress responses of ballasted track with high-speed train loads, a parametric study is performed in this section based on the Qin-Shen HSR 2.5D FE model. Five observation points located vertically beneath the rail, marked *A*, *B*, *C*, *D*, and *E* in Fig. 4, are chosen, at depths below the top of the sub-ballast layer of 0 m (top of the sub-ballast layer), 0.4 m (top of the subgrade), 1.7 m (middle of the subgrade), 3.0 m (the surface of ground), and 6.0 m (3.0 m below the ground).

### 4.1 Dynamic stresses within subgrade and underlying soils

Fig. 6 shows the time-histories of dynamic vertical stresses at different depths beneath the rail calculated for train speeds of 250 km/h and 420 km/h. For a train speed of 250 km/h, the maximum value of dynamic stress is 69.0 kPa at location *A*, 49.5 kPa at location *B*, 29.0 kPa at location *C*, and 11.0 kPa at location *D*; at a depth of 3.0 m below the ground surface (location *E*), the maximum stress reduces to 5.5 kPa. For a train speed of 420 km/h, the maximum values of dynamic stresses are 100.0 kPa, 68.0 kPa, 44.0 kPa, 18.0 kPa, and 9.0 kPa for the five locations, respectively. The amplitudes of dynamic stress show a dramatic increment with the train speed, especially inside the track substructure.

Fig. 7 shows the attenuation of the vertical dynamic stress amplitudes with the depth from the surface of the sub-ballast layer. Computational results are shown for five different speeds. For comparison, results from the Boussinesq approach are also given.

It can be seen that the track substructure introduces considerable attenuation of the dynamic stress induced by moving train traffic loads. The dynamic stress transmitted to the ground surface (at 3.0 m depth) is less than 20% of the magnitude of the stress at the surface of the substructure (0 m). The stress attenuation rate is quite high inside the sub-ballast layer, and then slows down in the subgrade layer. Higher train speeds induce larger dynamic stress in the substructure, but the dynamic stress in the ground shows a much smaller difference. These results indicate that the function of the substructure in reducing the stresses transmitted to the ground to avoid track excessive settlement is very effective, at any train speeds. In Fig. 7, the Boussinesq approximation yields higher stresses than the computational results of 2.5D FE method when the depth is lower than 1.0 m, and smaller stresses when the depth became deeper, especially at

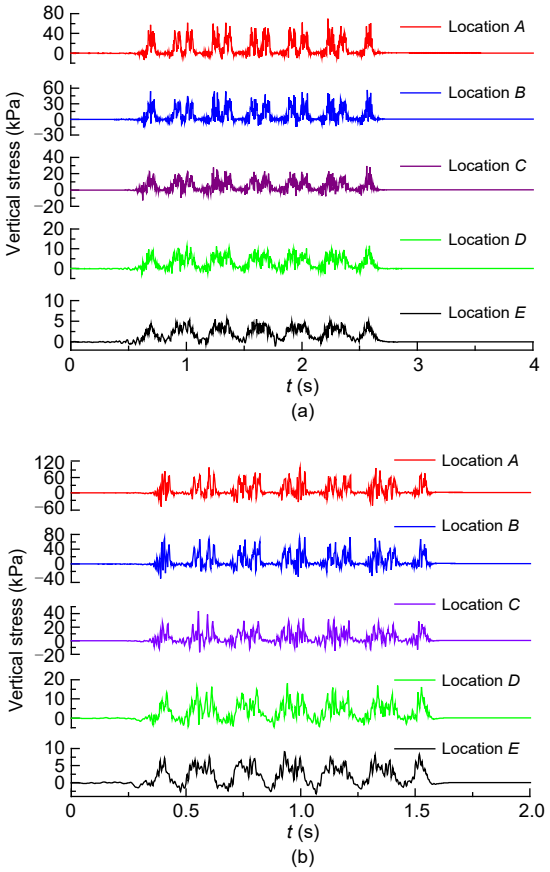


**Fig. 6 Time-histories of dynamic vertical stresses at different depths: (a) $c$=250 km/h; (b) $c$=420 km/h**

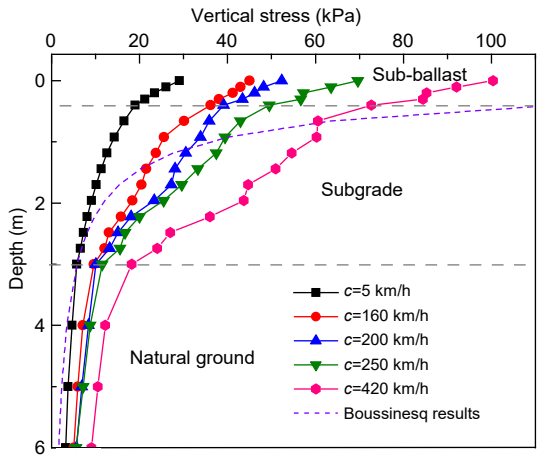


**Fig. 7 Attenuation of dynamic vertical stress amplitudes with depth below the ballast layer**

high speeds. This indicates that the effect of the multi-layered substructures and train speeds should be considered when determining the vertical stress induced by the train traffic loads.

## 4.2 Development of dynamic responses with train speed

Fig. 8 shows the maximum vertical displacements at location $A$ as a function of train speed. It shows that the critical speed of the Qin-Shen HSR model is about 440 km/h (122.2 m/s), which is higher than the minimum Rayleigh wave speed of the sub-soil layers (101.2 m/s) owing to the presence of the stiffer track substructure.

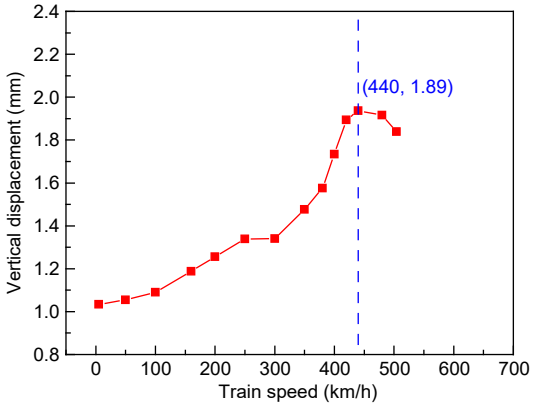


**Fig. 8 Maximum vertical displacements at location $A$ plotted as a function of train speed**

The China Academy of Railway Science (CARS) proposed an empirical formulation to calculate the dependence of dynamic vertical stress in the substructure on train speed based on many field measurements (NRA, 2014), which has been used for HSR design and maintenance:

$$\sigma_{\mathrm{d}}=\sigma_{\mathrm{p}}(1+\alpha c), \tag{21}$$

where $\sigma_{\mathrm{d}}$ is the dynamic stress, $\sigma_{\mathrm{p}}$ is the dynamic stress under the quasi-static condition, and $\alpha$ characterizes the effect of train speed on dynamic stress. For an HSR, the value of $\alpha$ is set as 0.003.

Fig. 9 plots the maximum stress versus train speed an HSR together with the measured values and empirical values from Eq. (21). The good agreement between measurement results and 2.5D FE method results further validates the ability of the model to determine the dynamic stress properly in the ballasted track, within the range from low to high train speeds.

At low speeds (≤100 km/h), the numerical results for the smooth track are close to those of the irregular

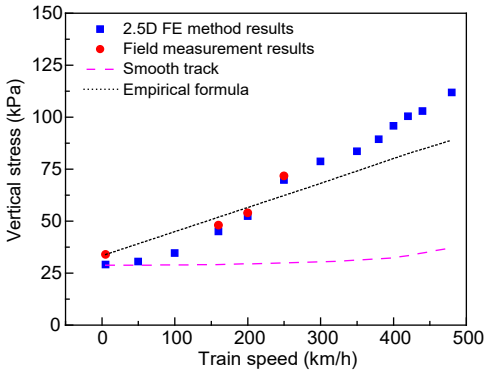


**Fig. 9 Dependence on the train speed of vertical dynamic stress magnitudes at location *A***

rail, which also correspond closely to the field measurement results. In other words, at low speeds, models only accounting for a smooth track can give reasonable results in terms of dynamic stress. However, at higher speeds, the dynamic stresses determined using the smooth track model are far below the measurement results, which means that for HSRs, models considering smooth rails only do not give acceptable results, and the track irregularity must be considered.

Meanwhile, when the train speed is less than 200 km/h, the dynamic stresses at location *A* obtained from the 2.5D FE method, considering the measured track irregularity PSD, are smaller than the values obtained from the empirical formulation in Eq. (21); however, as the train speed increases above 250 km/h, the computed dynamic stresses exceed the empirical values. Moreover, it is important to notice that the track irregularity of the Qin-Shen HSR was measured prior to the start of official operation. After several years of train operation, the track irregularity will increase, leading to higher dynamic stresses, which possibly may exceed the empirical formulation value even at lower speeds. That would lead to further acceleration of track degradation and cause excessive permanent deformation in the track substructure. Therefore, in the design and maintenance of HSRs, an empirical formulation considering only the effect of train speed is not accurate enough; the dynamic amplification effect caused by track irregularity should also be taken into account.

### 4.3 Effect of rail pad stiffness and damping

Rail pads connect the rail and track substructure. Thus, it is important to understand the dynamic stresses related to the stiffness and damping effects of rail pads. Four categories of rail pad stiffness (very soft, soft, medium, and hard) are considered to find out the effect of rail pad stiffness on the dynamic stress. The stiffnesses of very soft, soft, medium, and hard rail pads are considered as 10, 20, 100, and 1000 MN/m$^2$, respectively (Ju et al., 2018; Khajehdezfuly, 2019). The damping of all rail pads is considered as 10 kN·s/m$^2$. Fig. 10 shows the dynamic stress time-history curves at location *A* and location *D* at a train speed of 250 km/h. It shows that the amplitudes of dynamic stress significantly increase when the rail pad stiffness changes from hard to very soft. The maximum dynamic stresses at location *A* of four cases are 89, 70, 64, and 64 kPa for rail pad stiffnesses of 10, 20, 100, and 1000 MN/m$^2$, respectively. When the stiffness changes from medium to very soft, the dynamic stress amplitude at location *A* increases about 40%. As for the dynamic stresses at location *D*, the maximum values of the four cases are 35, 26, 22, and 21 kPa, respectively. The amplitude increases about 60% when rail pad stiffness changes from medium to very soft.

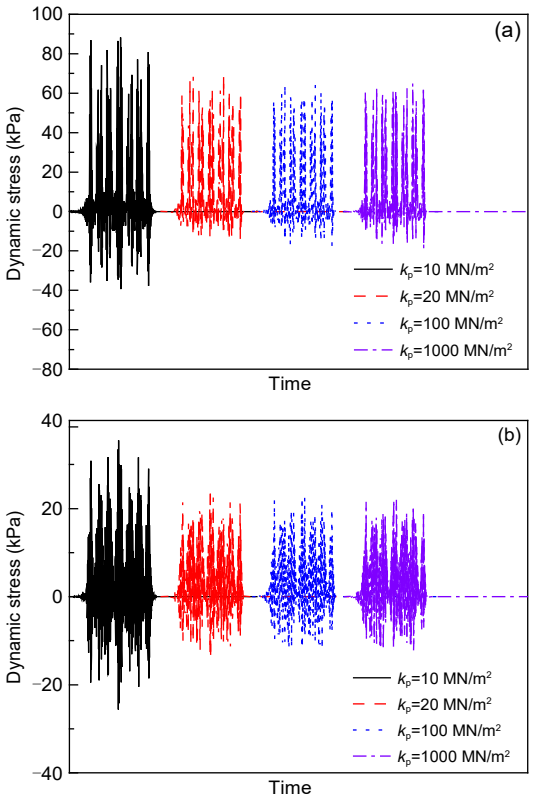


**Fig. 10 Time-history curves of dynamic stress with different rail pad stiffnesses at train speed of 250 km/h at location *A* (a) and location *D* (b)**

Four categories of rail pad damping with the values of 10, 20, 30, and 200 kN·s/m$^2$ are also considered to find out the effect of rail pad damping on the dynamic stress. Two analyses are conducted with one considering the stiffness of all rail pads as 10 MN/m$^2$ and the other considering it as 100 MN/m$^2$. Fig. 11a shows the dynamic stress time-history curves at location *A* with the rail pad damping values of 10, 20, 30, and 200 kN·s/m$^2$ for a fixed pad stiffness of 10 MN/m$^2$. It shows that rail pad damping can have a significant influence on the dynamic stress amplitudes when the rail pad is very soft. The damping effect of rail pad on dynamic stress is quite remarkable when the rail pad damping is in the range of 10 to 30 kN·s/m$^2$. However, when the rail pad is medium stiff (Fig. 11b), the rail pad damping has only a slight effect on the dynamic stress. This phenomenon was also found in some vibration research (Lei and Zhang, 2011; Dai et al., 2016).

### 4.4 Effect of track irregularity

Japan has the longest history of operation of high-speed railways, and also has rich research on the management standards for track irregularities. In this section, the management standard of Japanese Shinkansen longitudinal track irregularity has been adopted (Tanaka et al., 2011). In the criteria, the longitudinal track irregularity has been divided into five levels. Level I represents a newly-built railway line that is qualified to be used. Level II is a railway line needing some scheduled maintenance. At Level III, the comfort of passengers is affected by track irregularity, and the railway line needs maintenance. At Level IV, the safety of the train is threatened by the track irregularity. At Level V, the train speed must be reduced. The wavelengths and amplitudes of the management standard of Japanese Shinkansen longitudinal track irregularity for each level are listed in Table 4.

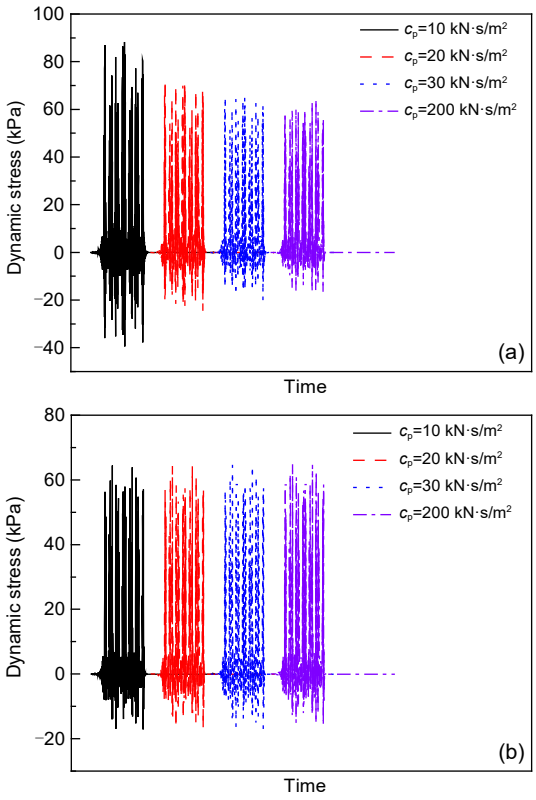


**Fig. 11 Time-history curves of dynamic stress with different rail pad stiffnesses at train speed of 250 km/h: (a) very soft; (b) medium**

**Table 4 Wavelengths and amplitudes of the management standard of Japanese Shinkansen longitudinal track irregularity (>160 km/h) (Tanaka et al., 2011)**

| Irregularity level | Wavelength (m) | Amplitude (mm) |
|---|---|---|
| Level I | 10 | ⩽4 |
| Level II | 10 | 6 |
| Level III | 10 | 7 |
| Level IV | 10 | 10 |
| Level V | 10 | 15 |

Based on the proposed 2.5D FE model of Qin-Shen HSR with the "Pioneer" train, the dynamic responses of ballasted track considering the five levels of longitudinal track irregularities are investigated.

#### 4.4.1 Dynamic responses

Fig. 12a illustrates the maximum displacement response versus train speed at location *A*. It can be seen that track irregularity substantially affects the track displacement. The displacements under the same track irregularity increase with increasing train speed, especially when that exceeds 350 km/h. For the same wavelength of 10 m, larger irregularity amplitudes produce higher displacement levels, and more significant growth of vibration will be induced by moving train traffic loads. The displacement obtained using the measured Qin-Shen HSR track irregularity spectrum is also plotted. Since the Qin-Shen HSR irregularity was measured before the railway line was officially used, the corresponding displacement vibrations are quite close to the value of the initial Level I when the train speed remains below 160 km/h. When the train speed exceeds 160 km/h, the displacement responses

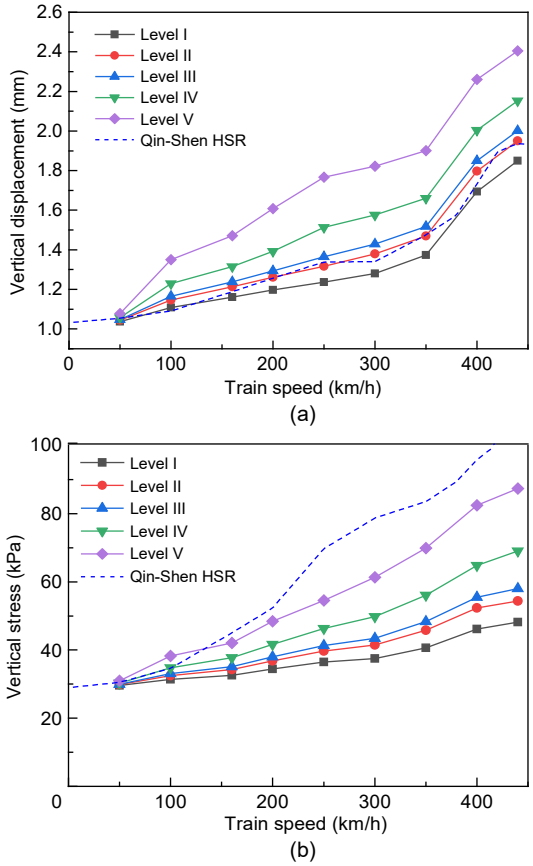


**Fig. 12 Displacement responses (a) and stress responses (b) versus train speed at location *A* under different track irregularity levels and from the measurement of Qin-Shen HSR**

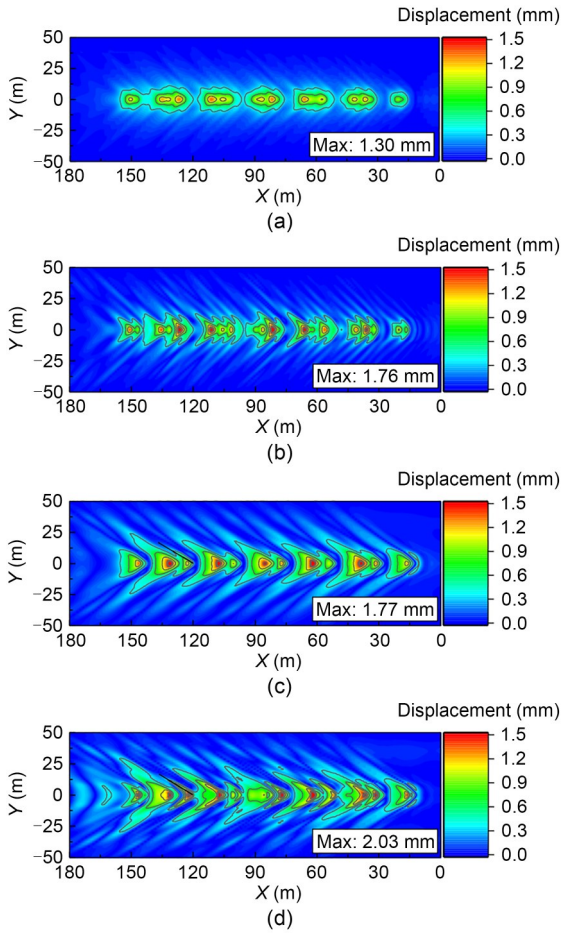


**Fig. 13 Displacement distribution induced by moving train load in *x*-*y* plane: (a) *c*=250 km/h, Level I; (b) *c*=250 km/h, Level V; (c) *c*=440 km/h, Level I; (d) *c*=440 km/h, Level V**

are quite close to the values of Level II. This indicates the newly-built Qin-Shen railway line was in a good condition and would meet the Japanese Shinkansen vibration requirement for newly-built lines. Fig. 12b illustrates the stress response versus train speed at location *A*. The stress responses increase considerably with train speed. For each track irregularity level, the growth rate does not show significant change with the train speed. The stress responses under the measured track irregularity PSD from Qin-Shen HSR are also plotted in the figure. Unlike the displacement responses, the stresses considering the measured track irregularity PSD are larger than those obtained using the Japanese Shinkansen irregularity levels when the train speed exceeds 100 km/h. It suggests that the stress response of Qin-Shen HSR has a different dependence on the PSD of the irregularity compared to the displacement response.

Fig. 13 shows the vibration propagation induced by each wheelset during the passage of a whole train in the *x*-*y* plane with *z*=3 m (natural ground surface) at various train speeds at Level I and Level V when the track irregularity wavelength is 10 m. At a relatively low train speed, vibration is mainly confined at the ground near the axle positions, but when the train speed reaches the critical speed, vibration wave propagation is in reverse from the train moving direction and forms a shock wave in the ground known as a Mach cone. The Mach cone grows with the development of track irregularity.

Fig. 14 shows the stress propagation induced by each wheelset during the passage of a whole train in the *x*-*y* plane with *z*=3 m at various train speeds at Level I and Level V when the track irregularity wavelength is 10 m. A fierce dynamic stress amplification phenomenon can be observed when the track irregularity changes from Level I to Level V for each train speed. The acting horizontal scopes of dynamic stress

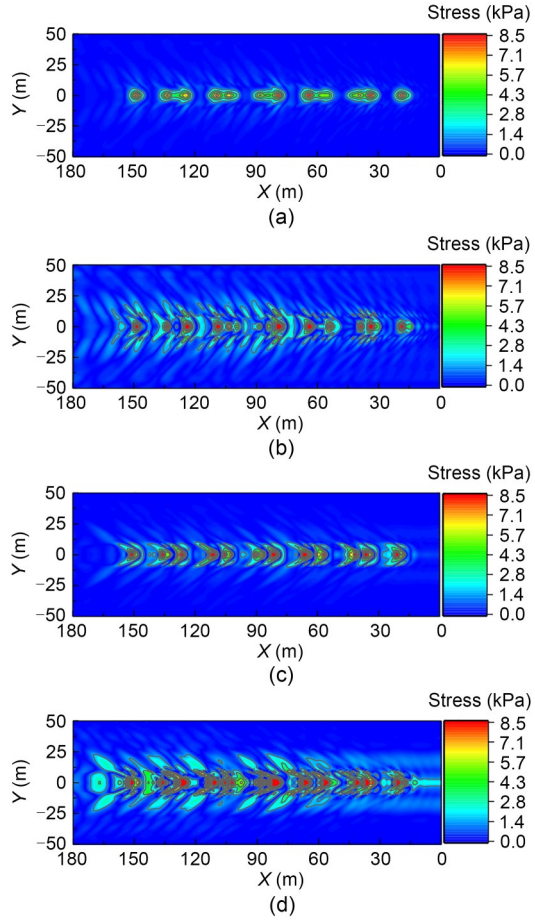


**Fig. 14 Stress distribution induced by moving train load in *x*-*y* plane: (a) *c*=250 km/h, Level I; (b) *c*=250 km/h, Level V; (c) *c*=440 km/h, Level I; (d) *c*=440 km/h, Level V**

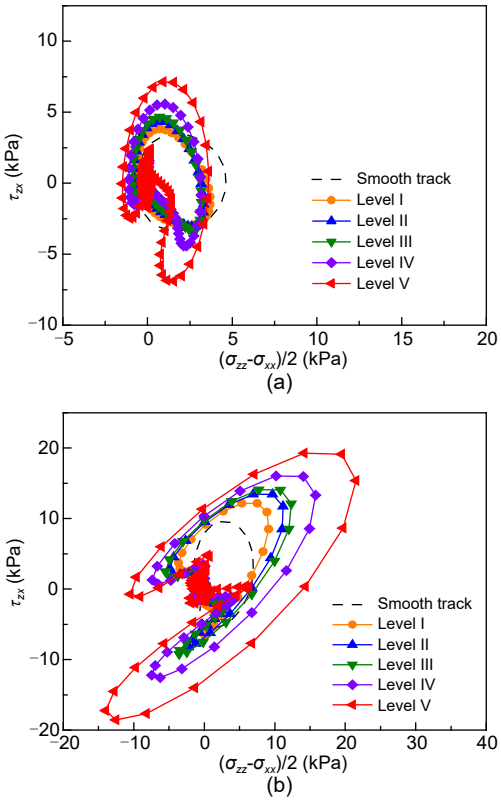


**Fig. 15 Principal stress axis rotation at various speeds in response to longitudinal track irregularity levels at location *C*: (a) *c*=250 km/h; (b) *c*=440 km/h. $\sigma_{xx}$ is the horizontal stress; $\sigma_{zz}$ is the vertical stress; $\tau_{zx}$ is the shear stress**

at the natural ground also increase with the development of track irregularity.

### 4.4.2 Stress paths

For traffic loading, a soil element is subjected to stress paths with principal stress rotation as well as deviatoric stress variation (Ishihara and Towhata, 1983). In this section, the effects of track irregularity on the rotation of principal stress and the stress paths are investigated using the 2.5D FE model of the Qin-Shen HSR. To obtain the dynamic stress components of the soil elements, loads corresponding to a quarter car model of a "Pioneer" train (Table 1) were used. The stress path and principal stress axis rotation in the *x*-*z* plane were analyzed.

Fig. 15 shows the relationship between the dynamic deviator stress and shear stress in the subgrade (location *C*) under a single load moving at different speeds considering different longitudinal track irregularity levels.

The stress paths for cases with track irregularity under a single load show more than one stress rotation; however, most of the rotations have small stress amplitudes. The shear stress levels for the dominant rotation increase dramatically in the subgrade with the development of track irregularity. The shapes of the curves are similar for each track irregularity level when the load speed is smaller than 250 km/h. However, when the load speed arrives at the critical speed, the shapes of curves vary significantly. This makes the stress path adopt a "pear" shape when the load speed is much lower than the critical speed; conversely, it becomes more distorted when the speed reaches the critical speed.

Fig. 16 shows the *p*-*q* stress path curves, on the graph of $p$ ($p$=($\sigma_1$−$\sigma_3$)/2, where $\sigma_1$ and $\sigma_3$ are the major and minor principal stresses, respectively) against $q$ ($q$=($\sigma_1$+$\sigma_3$)/2), for the soil elements at location *C* during the passage of a single load at 250 km/h and at 440 km/h

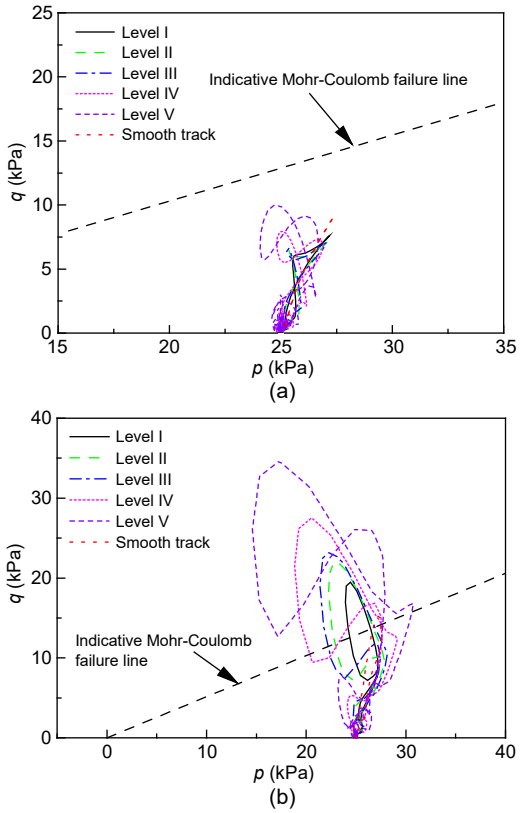


**Fig. 16 Stress path curves at various depths in response to longitudinal track irregularity levels at location *C*: (a) *c*= 250 km/h; (b) *c*=440 km/h**

while considering different longitudinal track irregularity levels. The stress paths are plotted on the basis of in situ conditions corresponding to an initial vertical stress of 20 kPa due to self-weight $K_0$=1.0. An indicative Mohr-Coulomb failure line is also plotted assuming an effective angle of friction of 31° (Grabe, 2002). This line is plotted for illustrative purposes only. Fig. 16 shows that the stress state moves closer to the failure line as the load speed is increased, and that the indicative failure envelope could be reached by a soil element in the subgrade at the critical speed. The levels of longitudinal track irregularity will affect the location of the stress paths relative to the indicative failure line. Increasing the levels will move the stress paths closer to the indicative failure line, increasing the likelihood of failure, especially at high speed.

## 5 Conclusions

Understanding the dynamic stresses induced in the track substructure and underlying soil by moving train loads is essential to the sustainable design and maintenance of HSRs. In this paper, an efficient 2.5D analysis method for a ballasted railway, comprising vehicle, track, substructure, and underlying soil, has been derived. It is used to investigate the dynamic stress response during train passages at various speeds, highlighting the dynamic stress responses when the train speed approaches the critical speed. The main conclusions can be summarized as follows:

1. The analysis of the stress attenuation with depth reveals that the substructure is effective in reducing the stresses transmitted to the ground. The Boussinesq approximation cannot consider the effect of multi-layered substructures and train speeds in determining the vertical stress induced by the train traffic loads.

2. At low speed (≤100 km/h), the analysis model for assessing dynamic stress response under train moving loads can be based on the assumption of a smooth track and can give acceptable results. However, in the design and maintenance of HSRs, an empirical formulation considering only the effect of train speed is not accurate enough, and the dynamic amplification effect caused by track irregularity should also be taken into account.

3. When the stiffness of the rail pad is reduced, an increase in the damping value can effectively decrease the dynamic stress transmitted to the subgrade.

4. As the track irregularity develops, larger stress amplitudes will be induced by the moving train load, and significant stress levels will propagate deeper. Consequently, the soil will suffer from large stresses, which are more likely to cause soil deformation.

5. The track irregularity can induce many principal stress rotations even under a simple single moving load. Increasing the levels of longitudinal track irregularity will move the stress paths closer to the indicative failure line, increasing the likelihood of failure, especially at high speed.

## Acknowledgments

This work is supported by the National Natural Science Foundation of China (No. 52108308), the Start-up Fund of Fuzhou University (No. 0050-510086 GXRC-20024), the Young Scientist Program of Fujian Provincial Natural Science Foundation of China (No. 2020J05107), the Foundation of MOE Key Laboratory of Soft Soils and Geoenviromental Engineering, Zhejiang University, China (No. 2020P05).

## Author contributions

Xue-cheng BIAN designed the research. Jing HU processed the corresponding data and wrote the first draft of the manuscript. Jing HU and Xue-cheng BIAN revised and edited the final version.

## Conflict of interest

Jing HU and Xue-cheng BIAN declare that they have no conflict of interest.

## References

AREA (American Railway Engineering Association), 1996. Manual for Railway Engineering. AREA, Washington DC, USA.

Auersch L, 2008. The effect of critically moving loads on the vibrations of soft soils and isolated railway tracks. *Journal of Sound and Vibration*, 310(3):587-607. https://doi.org/10.1016/j.jsv.2007.10.013

Bian XC, Chao C, Jin WF, et al., 2011. A 2.5D finite element approach for predicting ground vibrations generated by vertical track irregularities. *Journal of Zhejiang University-SCIENCE A (Applied Physics & Engineering)*, 12(12):885-894. https://doi.org/10.1631/jzus.A11GT012

Bian XC, Jin WF, Jiang HG, 2012. Ground-borne vibrations due to dynamic loadings from moving trains in subway tunnels. *Journal of Zhejiang University-SCIENCE A (Applied Physics & Engineering)*, 13(11):870-876. https://doi.org/10.1631/jzus.A12ISGT5

Bian XC, Jiang HG, Chang C, et al., 2015. Track and ground vibrations generated by high-speed train running on ballastless railway with excitation of vertical track irregularities. *Soil Dynamics and Earthquake Engineering*, 76:29-43. https://doi.org/10.1016/j.soildyn.2015.02.009

Bian XC, Cheng C, Jiang JQ, et al., 2016. Numerical analysis of soil vibrations due to trains moving at critical speed. *Acta Geotechnica*, 11(2):281-294. https://doi.org/10.1007/s11440-014-0323-2

Bian XC, Hu J, Thompson D, et al., 2019. Pore pressure generation in a poro-elastic soil under moving train loads. *Soil Dynamics and Earthquake Engineering*, 125:105711. https://doi.org/10.1016/j.soildyn.2019.105711

Brenner SC, Scott LR, 2008. The Mathematical Theory of Finite Element Methods. Springer, New York, USA.

Cai Y, Yu HS, Wanatowski D, et al., 2013. Noncoaxial behavior of sand under various stress paths. *Journal of Geotechnical and Geoenvironmental Engineering*, 139(8):1381-1395. https://doi.org/10.1061/(ASCE)GT.1943-5606.0000854

Cai YQ, Guo L, Jardine RJ, et al., 2017. Stress–strain response of soft clay to traffic loading. *Géotechnique*, 67(5):446-451. https://doi.org/10.1680/jgeot.15.P.224

Choi J, 2014. Retracted: influence of track support stiffness of railway tracks on track impact factor. *Journal of Engineering Mechanics*, 140(8):04014052. https://doi.org/10.1061/(ASCE)EM.1943-7889.0000744

Dai F, Thompson DJ, Zhu Y, et al., 2016. Vibration properties of slab track installed on a viaduct. *Proceedings of the Institution of Mechanical Engineers, Part F: Journal of Rail and Rapid Transit*, 230(1):235-252. https://doi.org/10.1177/0954409714533790

Grabe PJ, 2002. Resilient and Permanent Deformation of Railway Foundations under Principal Stress Rotation. PhD Thesis, University of Southampton, Southampton, UK.

Heath DL, Waters JM, Shenton MJ, et al., 1972. Design of conventional rail track foundations. *Proceedings of the Institution of Civil Engineers*, 51(2):251-267. https://doi.org/10.1680/iicep.1972.5952

Hu J, Bian XC, Jiang JQ, 2016. Critical velocity of high-speed train running on soft soil and induced dynamic soil response. *Procedia Engineering*, 143:1034-1042. https://doi.org/10.1016/j.proeng.2016.06.102

Hu J, Bian XC, Xu WC, et al., 2019. Investigation into the critical speed of ballastless track. *Transportation Geotechnics*, 18:142-148. https://doi.org/10.1016/j.trgeo.2018.12.004

Ishihara K, Towhata I, 1983. Sand response to cyclic rotation of principal stress directions as induced by wave loads. *Soils and Foundations*, 23(4):11-26. https://doi.org/10.3208/sandf1972.23.4_11

Jin SH, Zeng ZP, Chen XF, et al., 2008. PSD analysis of slab track irregularity of Qinhuangdao-Shenyang dedicated passenger railway line. *Journal of Railway Science and Engineering*, 5(6):17-21 (in Chinese). https://doi.org/10.19713/j.cnki.43-1423/u.2008.06.005

Ju SH, Kuo HH, Ni SH, 2018. Vibration induced by moving cranes in high-tech buildings due to rail pad materials. *Shock and Vibration*, 2018:8623913. https://doi.org/10.1155/2018/8623913

Khajehdezfuly A, 2019. Effect of rail pad stiffness on the wheel/rail force intensity in a railway slab track with short-wave irregularity. *Proceedings of the Institution of Mechanical Engineers, Part F: Journal of Rail and Rapid Transit*, 233(10):1038-1049. https://doi.org/10.1177/0954409718825410

Lei XY, Zhang B, 2011. Analysis of dynamic behavior for slab track of high-speed railway based on vehicle and track elements. *Journal of Transportation Engineering*, 137(4):227-240. https://doi.org/10.1061/(ASCE)TE.1943-5436.0000207

Li DQ, Selig ET, 1998a. Method for railroad track foundation design. I: development. *Journal of Geotechnical and Geoenvironmental Engineering*, 124(4):316-322. https://doi.org/10.1061/(asce)1090-0241(1998)124:4(316)

Li DQ, Selig ET, 1998b. Method for railroad track foundation design. II: applications. *Journal of Geotechnical and Geoenvironmental Engineering*, 124(4):323-329. https://doi.org/10.1061/(asce)1090-0241(1998)124:4(323)

Li W, Bian XC, Duan X, et al., 2018. Full-scale model testing on ballasted high-speed railway: dynamic responses and accumulated settlements. *Transportation Research Record: Journal of the Transportation Research Board*, 2672(10):125-135. https://doi.org/10.1177/0361198118784379

Liu GR, Jerry SSQ, 2003. A non-reflecting boundary for analyzing wave propagation using the finite element method. *Finite Elements in Analysis and Design*, 39(5-6):403-417. https://doi.org/10.1016/S0168-874X(02)00081-1

Ngo NT, Indraratna B, Rujikiatkamjorn C, 2017. Simulation ballasted track behavior: numerical treatment and field application. *International Journal of Geomechanics*, 17(6): 04016130. https://doi.org/10.1061/(ASCE)GM.1943-5622.0000831

Nie ZH, 2005. Study on Vertical Dynamic Response of the Track/Subgrade in High-Speed Railway. PhD Thesis, Central South University, Changsha, China (in Chinese).

Nie ZH, Li L, Liu BC, et al., 2005. Testing and analysis on vibration of subgrade for Qinhuangdao-Shenyang railway. *Chinese Journal of Rock Mechanics and Engineering*, 24(6):1067-1071. https://doi.org/10.3321/j.issn:1000-6915.2005.06.030

NRA (National Railway Administration of the People's Republic of China), 2014. Code for Design of High Speed Railway, TB 10621-2014. NRA, Beijing, China (in Chinese).

Nussbaumer HJ, 1981. The fast Fourier transform. *In*: Nussbaumer HJ (Ed.), Fast Fourier Transform and Convolution Algorithms. Springer, Berlin, Germany, p.80-111.

Powrie W, Yang LA, Clayton CRI, 2007. Stress changes in the ground below ballasted railway track during train passage. *Proceedings of the Institution of Mechanical Engineers, Part F: Journal of Rail and Rapid Transit*, 221(2):247-262. https://doi.org/10.1243/0954409JRRT95

Powrie W, Priest JA, Clayton CRI, 2008. Recent research on railway track sub-base behaviour. *In*: Ellis E, Yu HS, McDowell G (Eds.), Advances in Transportation Geotechnics. CRC Press, London, UK, p.37-46.

Raymond GP, 1978. Design for railroad ballast and subgrade support. *Journal of the Geotechnical Engineering Division*, 104(1):45-60. https://doi.org/10.1061/AJGEB6.0000576

Sayeed A, Shahin MA, 2016. Three-dimensional numerical modelling of ballasted railway track foundations for high-speed trains with special reference to critical speed. *Transportation Geotechnics*, 6:55-65. https://doi.org/10.1016/j.trgeo.2016.01.003

Selig ET, Waters JM, 1994. Track Geotechnology and Substructure Management. Thomas Telford, London, UK.

Sheng X, Jones CJC, Petyt M, 1999. Ground vibration generated by a load moving along a railway track. *Journal of Sound and Vibration*, 228(1):129-156. https://doi.org/10.1006/jsvi.1999.2406

Shinozuka M, 2005. Simulation of multivariate and multidimensional random processes. *The Journal of the Acoustical Society of America*, 49(1B):357-368. https://doi.org/10.1121/1.1912338

Takemiya H, 2003. Simulation of track-ground vibrations due to a high-speed train: the case of X-2000 at Ledsgard. *Journal of Sound and Vibration*, 261(3):503-526. https://doi.org/10.1016/S0022-460X(02)01007-6

Takemiya H, Bian XC, 2005. Substructure simulation of inhomogeneous track and layered ground dynamic interaction under train passage. *Journal of Engineering Mechanics*, 131(7):699-711. https://doi.org/10.1061/(asce)0733-9399(2005)131:7(699)

Tanaka T, Higuchi T, Baba S, 2011. History of railway track maintenance of Japan from the viewpoint of regulations. *Journal of Japan Society of Civil Engineers, Ser. D2 (Historical Studies in Civil Engineering)*, 67(1):38-48 (in Janpanese). https://doi.org/10.2208/jscejhsce.67.38

Varandas JN, Paixão A, Fortunato E, et al., 2016. A numerical study on the stress changes in the ballast due to train passages. *Procedia Engineering*, 143:1169-1176. https://doi.org/10.1016/j.proeng.2016.06.127

Xiao JH, Juang CH, Wei K, et al., 2014. Effects of principal stress rotation on the cumulative deformation of normally consolidated soft clay under subway traffic loading. *Journal of Geotechnical and Geoenvironmental Engineering*, 140(4):04013046. https://doi.org/10.1061/(ASCE)GT.1943-5606.0001069

Yang LA, Powrie W, Priest JA, 2009. Dynamic stress analysis of a ballasted railway track bed during train passage. *Journal of Geotechnical and Geoenvironmental Engineering*, 135(5):680-689. https://doi.org/10.1061/(ASCE)GT.1943-5606.0000032

Yang YB, Hung HH, 2001. A 2.5D finite/infinite element approach for modelling visco-elastic bodies subjected to moving loads. *International Journal for Numerical Methods in Engineering*, 51(11):1317-1336. https://doi.org/10.1002/nme.208